Nanoscale Advances

ROYAL SOCIETY OF CHEMISTRY

PAPER

View Article Online
View Journal | View Issue

Cite this: *Nanoscale Adv.*, 2025, **7**, 231

First investigation of high-performance FeS-based $W_{18}O_{49}$ asymmetric supercapacitors operating at 1.6 V

Junaid Riaz, [a] Fawad Aslam,[b] Muhammad Arif,*[c] Tabasum Huma*[d] and Amina Bibi*[e]

Received 14th September 2024
Accepted 8th November 2024

DOI: 10.1039/d4na00767k

rsc.li/nanoscale-advances

This study presents a comprehensive evaluation of FeS–$W_{18}O_{49}$ composite electrodes, revealing their exceptional performance for supercapacitor applications. Fabricated *via* a wet-chemical method, the FeS–$W_{18}O_{49}$ composites demonstrated a high specific capacitance of 558 F g^{-1} at a current density of 1 A g^{-1}, showcasing their outstanding charge storage capabilities. The composites achieved an energy density of 89.77 W h kg^{-1} and a power density of 4950 W kg^{-1}, attributed to the synergistic effect between the excellent electrical conductivity of FeS and the redox activity of $W_{18}O_{49}$, which collectively enhance the electrode's electrochemical performance. Moreover, the FeS–$W_{18}O_{49}$ electrodes exhibited remarkable cycling stability, retaining 87.6% of their capacitance after 10 000 charge–discharge cycles. These findings underscore the potential of FeS–$W_{18}O_{49}$ composites to advance supercapacitor technology by improving energy storage capacity and extending cycle life.

1. Introduction

Due to their unique properties, such as high power and energy densities, supercapacitors have effectively bridged the gap between traditional batteries and capacitors in energy storage devices. In particular, micro-supercapacitors have attracted significant attention as a promising solution for powering wearable devices and wireless sensor networks.[1] Researchers are employing various methods to develop energy-efficient supercapacitors by optimizing both capacitance and the operating voltage window. However, these methods often face limitations due to issues such as low specific capacitance, low energy density, low power density and lack of cycling stability. To address these challenges, a shift toward the fabrication of asymmetric supercapacitors is proposed. The search for materials that can enhance asymmetric devices with superior chemical and physical properties such as high stability, low manufacturing costs, high power density, ease of synthesis, and elevated energy density remains in its early stages. Nevertheless, significant progress is being made. Considerable efforts are focused on identifying new materials that can be synthesized using simpler, more cost-effective manufacturing techniques to enable the commercialization of this technology.[2]

The majority of redox pseudocapacitors employ conductive polymers or TMOs as their electrode materials. Conductive polymers have a high specific capacitance. However, electroactive polymers are severely limited in their utilization due to material degradation from cycling-induced expansion and contraction.[3] Despite RuO_2's high pseudocapacitance value (up to 720 F g^{-1}) and robust electrical conductivity, its poisonous nature and high cost limit its commercial use.[4] Hence, there have been multiple initiatives to find alternative materials that are both more affordable and exhibit better capacitive behavior. Electrochemical capacitor materials such as MnO_2, NiO, Fe_2O_3, V_2O_3, $W_{18}O_{49}$, and CoO_2 have been the subject of substantial research due to this.[5–13] Even though metal oxides have been around for a while as electrochemical energy storage materials, it would be interesting to look at alternative electrode materials that are both inexpensive and have better performance. $W_{18}O_{49}$, for instance, is gaining attention as a promising future electrode material for electric double-layer capacitors (EDLCs) due to its low cost and high specific capacitance.[14] Due to the low specific capacitance, low energy density and cycling stability of TMOs, researchers mixed TMOs with different sulfides.[15] While tungsten-based electrode materials show significant promise for supercapacitor applications, achieving long-term cycling stability alongside high specific capacitance and rate capability remains a persistent challenge. The limited potential window of aqueous electrolytes further complicates the electrochemical performance of tungsten-based electrodes, potentially

[a]*Faculty of Material Science and Engineering, Kunming University of Science and Technology, Kunming 650093, China. E-mail: junaidriaz1990@gmail.com*
[b]*School of Physics & Electronics, Central South University, Hunan, China*
[c]*School of Physics and Electronic Information, Yunnan Normal University, 768 Juxian Street, Kunming 650500, Yunnan, China*
[d]*Faculty of Metallurgical and Energy Engineering, Kunming University of Science and Technology, Kunming 650093, China*
[e]*Department of Physics, Hazara University, Mansehra 21300, Pakistan. E-mail: aminamni11@gmail.com*

constraining their energy density.[16,17] To overcome these limitations and achieve higher energy densities, asymmetric supercapacitors (ASCs) are often employed, as they enable the extension of the operational voltage range of the device.

Iron sulfide (FeS) meets the key criteria for electrode materials in supercapacitors, including multiple oxidation states, long cycle life, low cost, abundance, and non-toxic nature. In recent decades, numerous efforts have focused on synthesizing FeS nanosheets to exploit these advantages. Developing new electrode materials like FeS is crucial due to their high demand, low cost, and large surface area, all of which are essential for advancing the commercialization of supercapacitor technology. Chodankar *et al.*[18] reported an MnO_2//MnO_2 symmetric supercapacitor with excellent energy storage performance within a voltage window of 1.6 V. Similarly, a supercapacitor device with a 1 V potential window was developed using a nickel cobaltite ($NiCo_2O_4$) nanowire array supported on a Ni foam electrode.[19]

This study presents a novel wet-chemical method for synthesizing FeS–$W_{18}O_{49}$ nanocomposite structures demonstrating exceptional electrochemical performance. These composites achieve a high specific capacitance of 558 F g^{-1} at a current density of 1 A g^{-1} and maintain outstanding cycling stability, retaining 87.3% of their initial capacity over 10 000 cycles at 10 A g^{-1}. The synergistic interaction between FeS and $W_{18}O_{49}$ enhances electrical conductivity, while the abundant active sites improve their overall electrochemical properties. An asymmetric supercapacitor constructed using FeS–$W_{18}O_{49}$||MnO_2 in a 3 M KOH electrolyte exhibits impressive energy and power densities of 89.77 W h kg^{-1} and 4950 W kg^{-1}, respectively, outperforming previously reported values. This research underscores the significant potential of the FeS–$W_{18}O_{49}$ nanocomposite in advancing energy storage solutions and contributes to developing more efficient and sustainable supercapacitor technologies (see Table 5).

2. Experimental section

2.1 Materials

The experimental procedure utilized the following materials: tungsten hexachloride (WCl_6), thioacetamide (C_2H_5NS), iron(III) chloride hexahydrate ($FeCl_3 \cdot 6H_2O$), ethanol, polyvinylidene fluoride (PVDF), *N*-methyl-2-pyrrolidone (NMP), nickel foam, manganese dioxide (MnO_2), and carbon black (CB). All chemicals were of analytical reagent grade and were procured from Sinopharm Chemical Reagent Co., Ltd, Beijing. These materials were used as received without any further purification.

2.2 Synthesis of $W_{18}O_{49}$

No further purification was necessary for the chemicals because they were all high-grade. 2 g of tungsten hexachloride (WCl_6) dissolved in 50 mL of ethanol is enough to make one urchin-shaped sphere of $W_{18}O_{49}$ material; then, the mixture was let to stand at room temperature for 30 minutes while stirring. This procedure produces a solution that is both transparent and yellow. After that, the solution was moved to a 100 mL Teflon-lined stainless steel autoclave and subjected to a temperature of 160 °C for 24 h. A dark-blue solid was produced by centrifugation, followed by washing with ultra-pure water and ethanol. The next step was to dry the solid at 60 °C in a vacuum.

2.3 Synthesis of FeS

To synthesize FeS nanoparticles, 6.8 g of thioacetamide (C_2H_5NS) and 5.8 g of iron(III) chloride hexahydrate ($FeCl_3 \cdot 6H_2O$) were dissolved in a mixture of 15 mL of deionized water and 6 mL of ethanol. To promote uniform mixing and facilitate the nucleation process, the solution was subjected to ultrasonication for 40 minutes. The resulting solution was then transferred into a 30 mL stainless-steel autoclave with a Teflon lining to ensure a controlled environment. Subsequently, the autoclave was sealed and placed in an oven, where it underwent heat treatment at 150 °C for 2 hours. This controlled thermal process enabled the formation of FeS nanoparticles with the desired morphology and crystallinity. Following the heat treatment, the FeS powder was thoroughly rinsed multiple times with ethanol and deionized water to remove any residual impurities or unreacted precursors. The purified FeS nanoparticles were then vacuum-dried at 60 °C for 4 hours to eliminate any remaining moisture, resulting in a stable and highly pure FeS product.

2.4 Synthesis of the FeS–$W_{18}O_{49}$ composite

According to Table 1, we created the FeS–$W_{18}O_{49}$ nanocomposite by combining 0.28 g of FeS with 0.56 g of $W_{18}O_{49}$. The use of 40 mL of methanol as a solvent simplified the procedure. To ensure that the FeS and $W_{18}O_{49}$ particles were mixed thoroughly, a methanol solution was added slowly while the mixture was agitated constantly. Sonication was applied after the components were well mixed. Because this method was so effective at agitating the fluid, the particles were distributed far more rapidly. The nanocomposite samples were then carefully dried until they were smooth. The temperature of the drying operation was kept constant at 80 °C. The samples were dried for 12 h to hasten the controlled evaporation of the solvents. After the nanocomposite material hardened, scientists could study it, characterize it, and potentially employ it as an electrode material for supercapacitors (Scheme 1).

2.5 Preparation of electrodes

In order to design the working electrode, nickel foil was pretreated sequentially with acetone, 3 M HCl, absolute ethanol and deionized water to ensure a clean surface. Then the slurry, prepared by mixing 80% synthesized material (active material),

Table 1 Composition of FeS–$W_{18}O_{49}$ with mass percent

Materials	Composition	FeS	$W_{18}O_{49}$	Methanol	Time	Temp.
FeS–$W_{18}O_{49}$	FeS–$W_{18}O_{49}$ (30–70)%	0.28 g	0.56 g	40 mL	12 h	80 °C

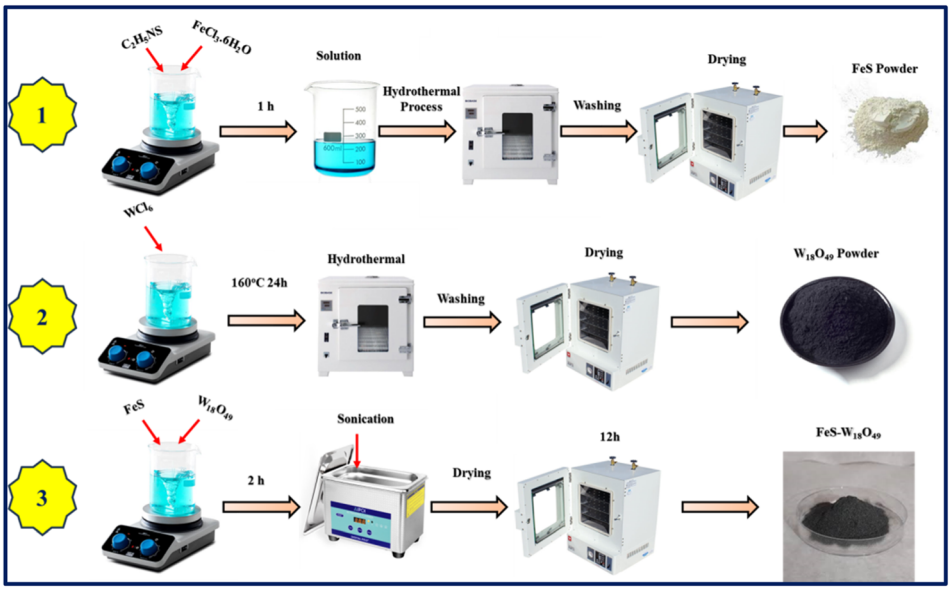

Scheme 1 Synthesis illustration of FeS, $W_{18}O_{49}$, and the FeS–$W_{18}O_{49}$ composite.

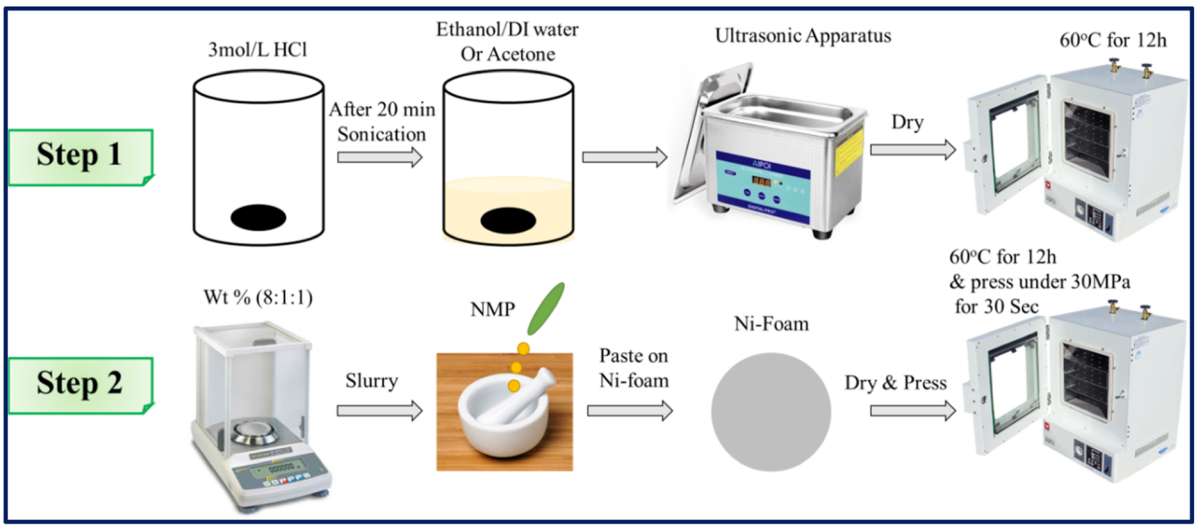

Fig. 1 Schematic diagram of preparation of electrodes.

10% carbon black and 10% poly(vinylidene)difluoride (PVDF), with *N*-methyl-2-pyrrolidone as solvent, was coated on 1 cm × 1 cm nickel foil (ring type). After pressing under 30 MPa pressure for 30 s, the electrode was dried in a hot air oven for 12 h at 60 °C. The mass of the fabricated electrode material was found to be 0.006 g (Fig. 1).

2.6 Characterization

This study aims to evaluate the performance of the FeS–$W_{18}O_{49}$ composite electrode in a three-electrode system using an aqueous 3 M KOH electrolyte solution over a potential range of −0.8 to 0.0 V. The electrochemical setup includes an Ag/AgCl reference electrode and a platinum wire as the counter electrode. The structural characterization of the synthesized samples was conducted using a Tongda TD-3500 X-ray diffraction (XRD) instrument equipped with a Cu Kα radiation source (λ = 1.5403 Å). This analysis enabled material verification, crystal structure determination, and phase identification. Surface morphology and structural analyses were performed using a JEOL JSM-7800F field emission scanning electron microscope (FESEM), while energy-dispersive X-ray spectroscopy (EDX) was utilized to confirm the elemental composition. The electrochemical properties of the nanocomposites were assessed using a DH7000C electrochemical workstation, employing techniques such as cyclic voltammetry (CV), galvanostatic charge–discharge (GCD) measurements, and electrochemical impedance spectroscopy (EIS). The testing utilized an Ag/AgCl reference electrode and a platinum foil counter

electrode in a 3 M KOH electrolyte solution. The specific capacitance, energy density, and power density were calculated using the relevant equations.[20]

$$C_s = \frac{I \times \Delta t}{m \times \Delta V} \quad (1)$$

$$E = \frac{C_s \times \Delta V^2}{7.2} \quad (2)$$

$$P = \frac{3600 \times E}{\Delta t} \quad (3)$$

where Δt, ΔV, and C_s represent the discharge time, voltage and capacitance, respectively.

3. Results and discussion

3.1 X-ray diffraction and SEM

Fig. 2a presents the X-ray diffraction (XRD) patterns of the synthesized $W_{18}O_{49}$, FeS, and FeS–$W_{18}O_{49}$ composite. The diffraction peaks of $W_{18}O_{49}$ correspond well with the Joint Committee on Powder Diffraction Standards JCPDS #71-2450, displaying peaks at 23.18°, 34.65°, 47.63°, and 55.75°, which are attributed to the (010), (114), (002), and (523) crystal planes, respectively. Similarly, the FeS sample aligns with JCPDS #75-2165, showing characteristic diffraction peaks at 29.9°, 30.4°, 34.7°, 43.2°, 53.1°, and 64.4°, corresponding to the (110), (004), (200), (114), (300), and (222) crystal planes, respectively. The XRD pattern of the FeS–$W_{18}O_{49}$ composite confirms the successful formation of the composite material, as it exhibits all the characteristic peaks of both FeS and $W_{18}O_{49}$. Additionally, the grain size of the synthesized materials was calculated using the Scherrer equation.

$$D = \frac{\kappa\lambda}{\beta \sin \theta} \quad (4)$$

where k is Scherrer's constant equal to 0.9; wavelength (λ) = 1.5418 Å; β is the full width at half maximum (FWHM) of the diffraction peak; and θ is the corresponding Bragg angle of the crystal plane.

The microstructural properties of the synthesized materials were meticulously analyzed using high-resolution field emission scanning electron microscopy (FESEM) with a JEOL JSM-7800F, as depicted in Fig. 2b–d. This advanced characterization technique provided detailed insights into the morphological features and the overall architecture of the materials. Fig. 2b illustrates the formation of $W_{18}O_{49}$ nanospheres with a distinctive urchin-like structure, characterized by a high degree of surface roughness and a radiating arrangement of nanoneedles. This unique morphology is known to offer a large surface area, which is beneficial for facilitating electrochemical reactions and enhancing energy storage capacity. Meanwhile, Fig. 2c demonstrates the synthesis of FeS nanoparticles with a sheet-like configuration. These nanosheets exhibit a thin and planar structure, which can promote effective ion diffusion and

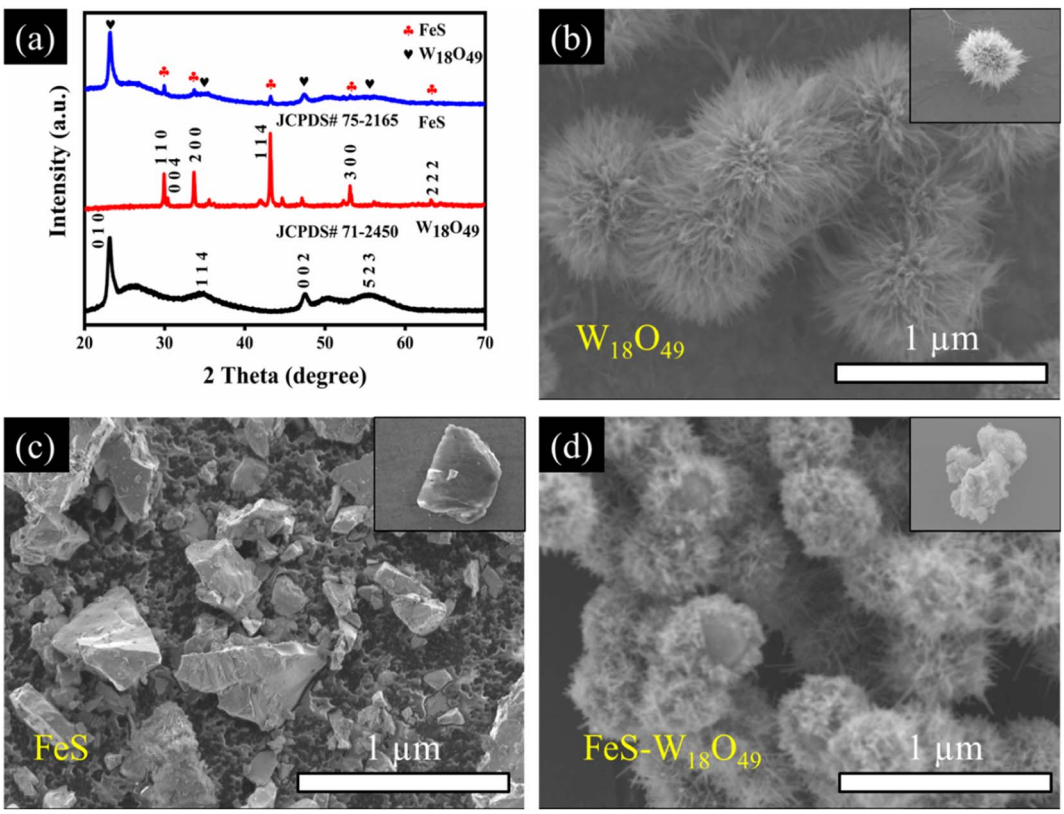

Fig. 2 XRD patterns of $W_{18}O_{49}$, FeS, and the FeS–$W_{18}O_{49}$ nanocomposite (a), accompanied by SEM images showcasing the morphology of (b) $W_{18}O_{49}$, (c) FeS, and (d) the FeS–$W_{18}O_{49}$ nanocomposite.

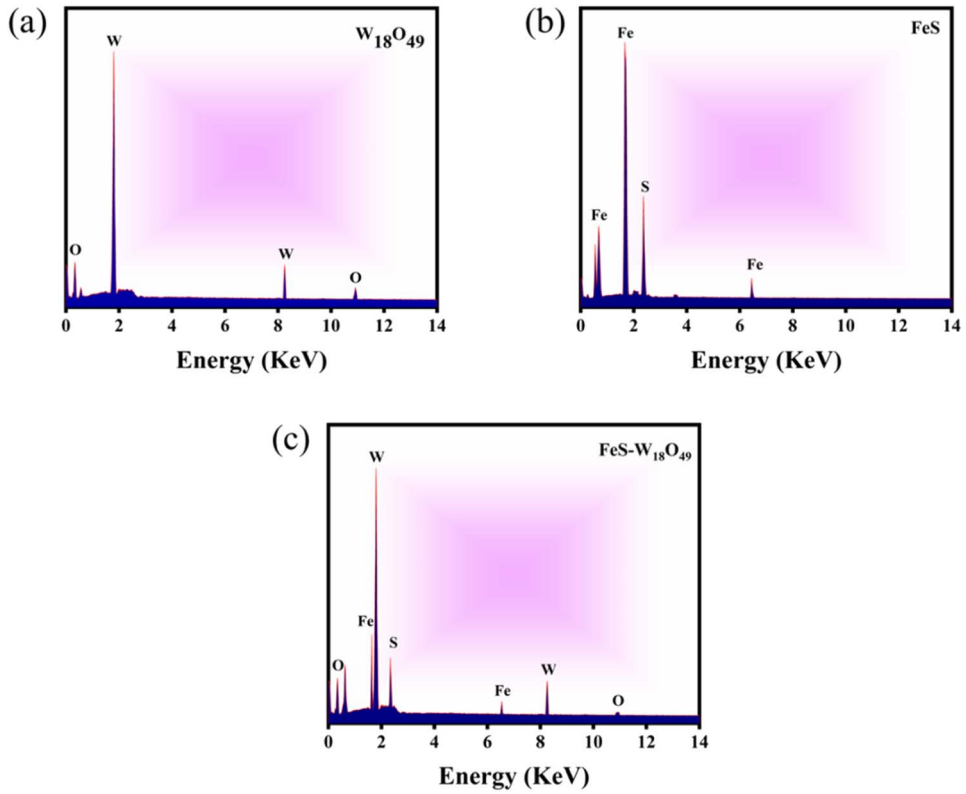

Fig. 3 Energy dispersive X-ray patterns of (a) $W_{18}O_{49}$, (b) FeS, and (c) the FeS–$W_{18}O_{49}$ composite.

improve the material's electrochemical performance. In Fig. 2d, the composite structure of FeS–$W_{18}O_{49}$ is revealed, where the FeS nanosheets are seen supporting and interspersing with the urchin-like $W_{18}O_{49}$ nanospheres. This unique arrangement suggests a strong interfacial interaction between FeS and $W_{18}O_{49}$, which can facilitate rapid electron transfer and enhance overall conductivity. The synergistic effect between these two components is likely to create more conductive pathways and improve charge storage capabilities, rendering the FeS–$W_{18}O_{49}$ composite more conductive and efficient than either component alone. These findings underscore the potential of the FeS–$W_{18}O_{49}$ composite as an advanced electrode material, capable of delivering enhanced performance metrics in terms of specific capacitance, rate capability, and cycling stability, making it a promising candidate for next-generation energy storage devices.

3.2 Elemental analysis

Further elemental analysis was carried out using Energy-Dispersive X-ray Spectroscopy (EDX) to confirm the successful formation of $W_{18}O_{49}$, FeS, and their composite. EDX detects characteristic X-ray emissions produced by the interaction of an electron beam with the sample, providing precise information on the elemental composition. As shown in Fig. 3a, the EDX spectrum of $W_{18}O_{49}$ reveals distinct peaks corresponding to tungsten (W) and oxygen (O), indicating the purity of the synthesized $W_{18}O_{49}$ nanospheres. Fig. 3b displays the characteristic peaks of iron (Fe) and sulfur (S), confirming the formation of FeS nanoparticles. Meanwhile, Fig. 3c shows peaks for Fe, S, W, and O, clearly verifying the successful synthesis of the FeS– $W_{18}O_{49}$ composite. The combined EDX results demonstrate that all expected elements are present in their respective samples, and the absence of any unexpected peaks confirms the purity and composition of the synthesized materials. This analysis further supports the formation of a well-integrated FeS–$W_{18}O_{49}$ composite, highlighting its potential advantages for enhanced electron transport and conductivity due to the synergistic interaction between FeS and $W_{18}O_{49}$.

4. Electrochemical characterization of energy storage capabilities

The electrochemical performance and energy storage properties of the FeS, $W_{18}O_{49}$, and FeS– $W_{18}O_{49}$ nanocomposite electrodes were systematically investigated using various analytical techniques, including cyclic voltammetry (CV), chronopotentiometry with a charge–discharge (CD) profile, and electrochemical impedance spectroscopy (EIS). Cyclic voltammetry (CV) was conducted in a three-electrode configuration to examine the electrochemical characteristics of these materials. Fig. 4 presents the voltammograms of FeS, $W_{18}O_{49}$, and the FeS–$W_{18}O_{49}$ composite electrodes, covering a potential range from −0.8 to 0.0 V. Comparative CV curves at a scan rate of 30 mV s^{-1} (Fig. 4a) demonstrate that the FeS–$W_{18}O_{49}$ composite exhibits the largest enclosed area under the curve, indicating its superior capacitance. The asymmetric shape of the CV curves reflects

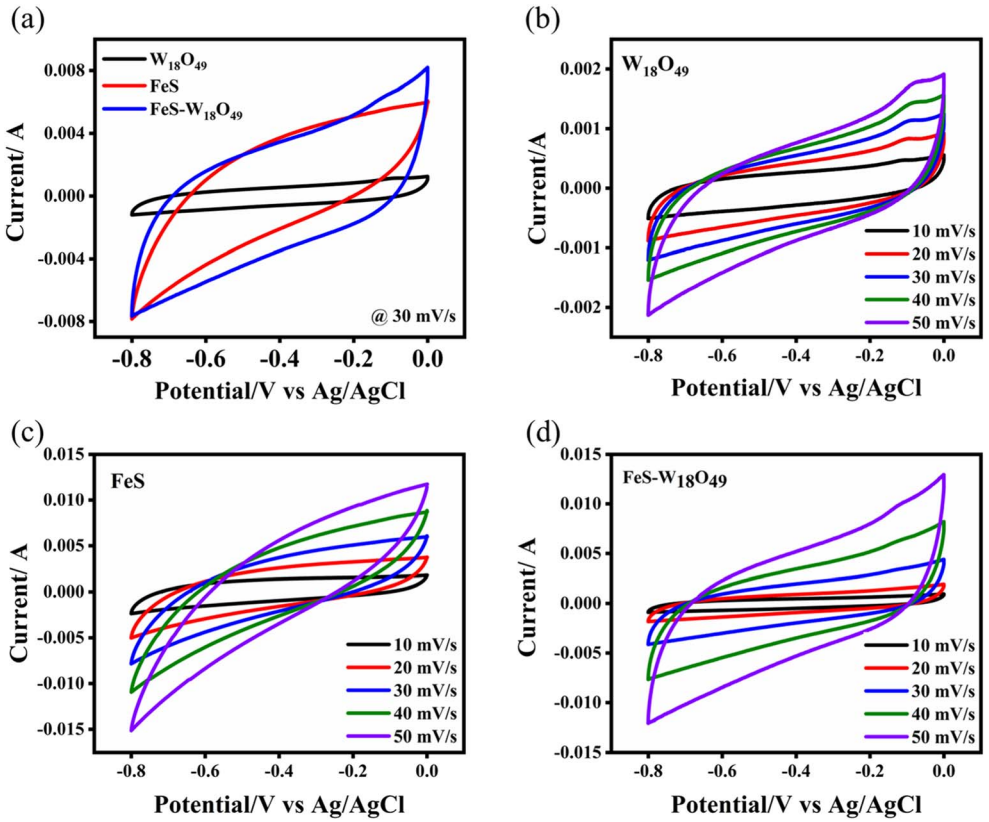

Fig. 4 (a) Cyclic voltammetry (CV) curves of $W_{18}O_{49}$, FeS and the FeS–$W_{18}O_{49}$ nanocomposite at a scan rate of 30 mV s^{-1}, and (b) $W_{18}O_{49}$, (c) FeS, and (d) the FeS–$W_{18}O_{49}$ composite at various scan rates.

the combined electrical double-layer capacitance (EDLC) characteristics of both FeS and $W_{18}O_{49}$ within the composite electrode. The larger loop area for the FeS–$W_{18}O_{49}$ electrode suggests enhanced energy storage performance, as the integration of FeS and $W_{18}O_{49}$ allows for a more efficient interaction of their capacitive mechanisms.

The capacitive enhancement in the FeS–$W_{18}O_{49}$ composite is primarily due to the synergistic effects between FeS and $W_{18}O_{49}$, which contribute to the overall twin-layer capacitance. The increased loop area in the CV curves confirms the effective combination of complementary capacitance processes, resulting in a notable rise in total capacitance. Furthermore, the cyclic voltammetry curves of the individual FeS and $W_{18}O_{49}$ electrodes, shown in Fig. 4b and c, exhibit a non-rectangular shape, suggesting a lack of pseudocapacitive behavior, typical of materials relying solely on EDLC. This characteristic capacitive behavior remains stable across different scan rates, as evidenced by the consistent progression of the CV loops, underscoring the robustness and reliability of these materials for energy storage applications.[21,22] FeS and $W_{18}O_{49}$ electrodes actively participate in redox processes by facilitating the intercalation and deintercalation of hydroxide ions (OH^-) from the KOH solution. For FeS, this process involves the reversible oxidation and reduction of iron ions (Fe^{2+}/Fe^{3+}), while for $W_{18}O_{49}$, it involves the redox cycling of tungsten ions between different oxidation states. The efficient and rapid movement of charge carriers within these materials is evidenced by the consistent shapes of the cyclic voltammetry (CV) curves across various scan rates, indicating stable electrochemical performance.

The reduced polarization of the FeS–$W_{18}O_{49}$ composite during charging and discharging enhances the effectiveness of energy storage and release. This suggests that the charge storage mechanism during electrochemical cycling includes both physical storage through electric double-layer capacitance (electrostatic charge separation at the electrode–electrolyte interface) and chemical storage through fast, reversible faradaic reactions involving the transfer of charge carriers (ions or electrons) to and from the surfaces of FeS and $W_{18}O_{49}$. This dual contribution enables the composite to achieve superior energy storage characteristics.

Moreover, the FeS CV curves have a predominantly rectangular form without any noticeable redox peaks, indicating that the material possesses a typical electrical double-layer capacitance (Fig. 4c).[23] As the scan rates increased, a consistent pattern emerged: the CV loops remained unchanged, and the positive and negative potentials mirrored each other, leading to excellent capacitive behaviour and rapid reversibility in the FeS electrode. Fig. 4d demonstrates the unique pattern of the cyclic voltammograms (CVs) of the FeS–$W_{18}O_{49}$ composite electrode, which exhibits both pseudocapacitive and double-layer behaviour, establishing the synergistic effects within each CV cycle.

Significantly, the FeS–$W_{18}O_{49}$ hybrid has a strongly improved current response throughout the whole range of voltage, surpassing the responses of both FeS and $W_{18}O_{49}$ electrodes. This enhanced response is substantiated by a much larger loop region in the cyclic voltammetry curve, demonstrating a substantially higher capacitance.

The charge storage mechanism of the electrode materials involves both the surface capacitance and diffusion-controlled processes. The contribution ratio can be calculated using the following equation:

$$i(V) = K_1 v + K_2 v^{1/2} \quad (5)$$

$$\frac{i}{v^{\frac{1}{2}}} = K_1 v^{1/2} + K_2 \quad (6)$$

The maroon integration area in Fig. 5b shows that the surface capacitance contribution is about 62% at a scan rate of 50 mV s^{-1}. As the scan rate increases from 10 mV s^{-1} to 50 mVs^{-1} (see Fig. 5a), the proportion of FeS–$W_{18}O_{49}$ increases from 26% to 62%. These findings suggest that at lower scan rates, the charge storage mechanism is mainly influenced by diffusion-controlled processes, when the ions have sufficient time to undergo redox reactions. In contrast, at higher scan rates, the effect of surface capacitance becomes more significant, resulting in a lower diffusion contribution due to the reduced time for ions to contact the electrode material.

The composite demonstrated a remarkable specific capacitance of 558 F g^{-1}, which can be ascribed to the synergistic interplay between FeS and $W_{18}O_{49}$. The charging process involves the release of protons from the electrolyte, which then interact with the electrode material, contributing to the storage of charge. In contrast, during the process of discharging, protons are released back into the electrolyte. Proton transfer kinetics are essential in aqueous environments, where hydrogen ions are vital for maintaining charge equilibrium in electrochemical processes. The increase in the capacitance of this system results from both faradaic and non-faradaic electrochemical reactions.

For the FeS and $W_{18}O_{49}$ components, the redox reactions occur as follows:

$$FeS + 2OH^- \rightarrow Fe(OH)_2 + S^{2-} \quad (7)$$

$$4Fe(OH)_2 + O_2 + 2H_2O \rightarrow 4Fe(OH)_3 \quad (8)$$

$$W_{18}O_{49} + OH^- \rightarrow K_xWO_3 + H_2O \quad (9)$$

Fig. 6 presents the impedance spectra of each electrode, illustrating both the real and imaginary components. The *x*-intercept on the real axis corresponds to the solution resistance (R_s), while the diameter of the semicircle reflects the charge transfer resistance (R_{ct}). The vertical line near the imaginary axis represents the electrolyte's diffusion resistance. The impedance plots for FeS, $W_{18}O_{49}$, and the FeS– $W_{18}O_{49}$ binary composite reveal similar trends (Fig. 6a). Notably, the FeS–$W_{18}O_{49}$ binary composite exhibits lower R_s and R_{ct} values compared to the individual FeS and $W_{18}O_{49}$ electrodes (Fig. 6b). This reduction in R_{ct} indicates enhanced conductivity of the composite electrode due to the incorporation of FeS into the $W_{18}O_{49}$ matrix. Conversely, the higher R_s and R_{ct} values observed for the pure $W_{18}O_{49}$ electrode suggest reduced conductivity and a larger electrode/electrolyte interfacial resistance. In contrast, the FeS–$W_{18}O_{49}$ composite demonstrates superior conductivity and improved capacitance performance relative to the pure $W_{18}O_{49}$ electrode (see Table 2).

To comprehensively evaluate the performance of the electrode materials, galvanostatic charge/discharge (GCD) experiments were conducted at various current densities ranging from 1 to 5 A g^{-1}. Fig. 7a presents a comparison of the electrode materials at a constant current density of 3 A g^{-1} over a voltage window of −0.8 to 0.0 V. The results indicate that the FeS–$W_{18}O_{49}$ binary composite exhibits a longer charge/discharge cycle duration compared to the pure FeS and $W_{18}O_{49}$ electrodes, suggesting enhanced electrochemical performance. Fig. 7b reveals a linear and stable charge–discharge profile for the $W_{18}O_{49}$ electrode that maintains its shape as the current density decreases, demonstrating its excellent cycling stability,

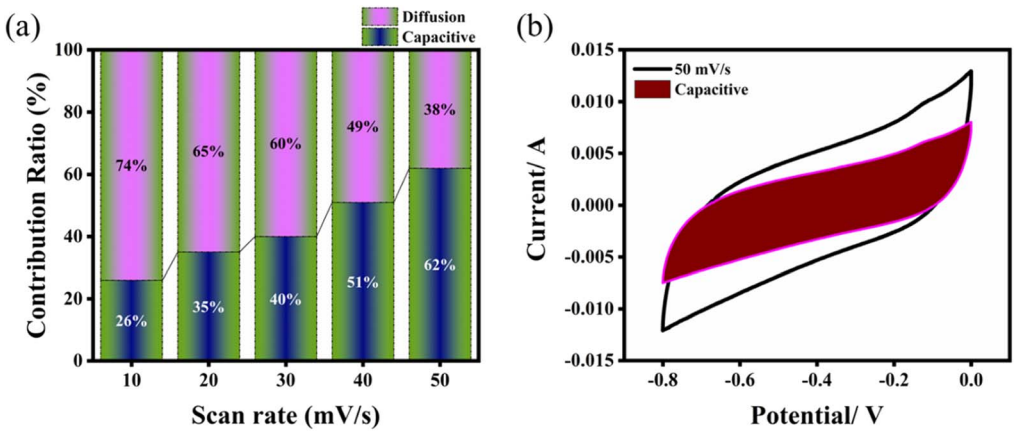

Fig. 5 (a) Contribution ratio of capacitance to total charge for FeS–$W_{18}O_{49}$ from 10 mV s^{-1} to 50 mV s; (b) contribution of the surface capacitance of FeS–$W_{18}O_{49}$ at 50 mV s^{-1}.

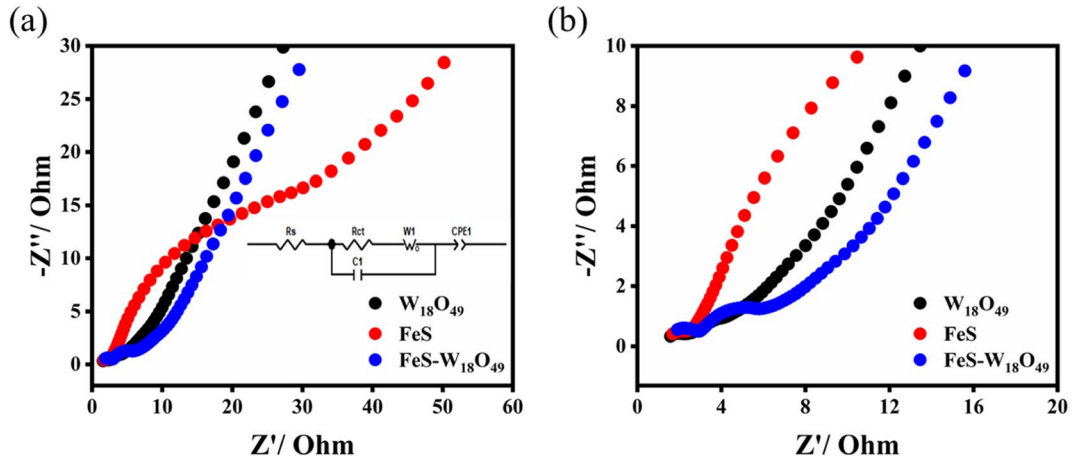

Fig. 6 (a) Nyquist impedance plot comparing the electrochemical impedance of $W_{18}O_{49}$, FeS, and the FeS–$W_{18}O_{49}$ composite, accompanied by an inset showing the equivalent circuit model. (b) Enlarged view of the high-frequency region for detailed analysis.

Table 2 Impedance plot analysis conducted using high-resolution zoom software

Materials	R_s (ohm)	R_{ct} (ohm)
FeS	1.58	2.73
$W_{18}O_{49}$	1.91	2.92
FeS–$W_{18}O_{49}$	1.67	2.56

reversibility, and substantial charge storage capacity. Conversely, the FeS electrode, as shown in Fig. 7c, displays substantial power delivery capabilities, as indicated by its charge–discharge characteristics. Fig. 7d further confirms that the FeS–$W_{18}O_{49}$ composite electrode outperforms both the individual FeS and $W_{18}O_{49}$ electrodes in terms of charge–discharge performance. As depicted in Fig. 7e, the FeS–$W_{18}O_{49}$ composite electrode achieves the highest capacitance, which can be attributed to the exceptional conductivity of the FeS component, resulting in superior overall electrochemical behavior. The nearly symmetrical charge–discharge curves of the FeS–$W_{18}O_{49}$ composite, with minimal distortion, indicate efficient charge storage dynamics. The discharge times were observed to be influenced by the current density, primarily due to the slower faradaic reactions occurring at lower current densities. This slow interaction between the electrode and

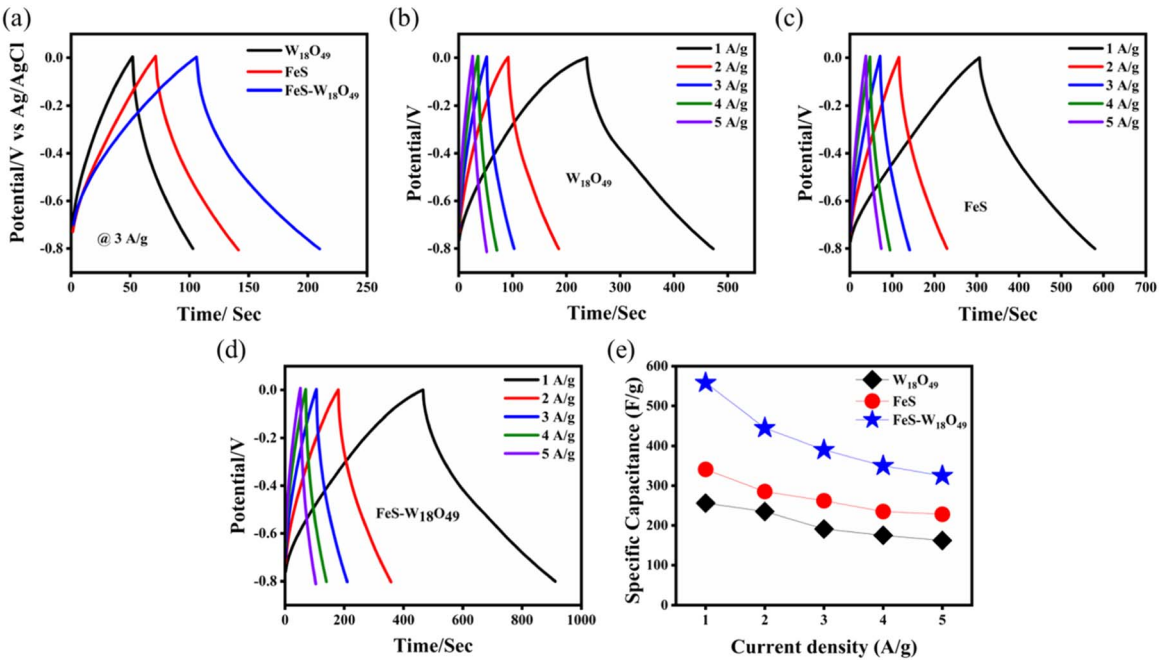

Fig. 7 (a) Comparative galvanostatic charge–discharge (GCD) performance of all electrodes at a current density of 3 A g^{-1}, GCD curves of (b) $W_{18}O_{49}$, (c) FeS, (d) FeS–$W_{18}O_{49}$ composite electrodes, and (e) specific capacitance values of all the prepared electrodes.

Table 3 Capacitance of the prepared electrode determined from the galvanostatic charge–discharge (GCD) curve

Current density (A g^{-1})	$W_{18}O_{49}$ (F g^{-1})	FeS (F g^{-1})	FeS–$W_{18}O_{49}$ (F g^{-1})
1	256	341	558
2	235	285	445
3	191	262	390
4	175	235	350
5	162	228	325

Table 4 Specific capacitance, energy density, and power density evaluated across various current densities

Current density (A g^{-1})	Specific capacitance (F g^{-1})	Energy density (W h kg^{-1})	Power density (W kg^{-1})
1	202	89.77	997.4
2	191	84.88	1997
3	129	57.33	2991
4	80	35.5	3993
5	62	27.5	4950

electrolyte points to the effective utilization of a high specific surface area. Table 3 provides detailed data on the capacitance values at different current densities.

To comprehensively evaluate the practical performance of the FeS–$W_{18}O_{49}$ electrode material in energy storage devices, we constructed an asymmetric supercapacitor (ASC) using MnO_2 as the anode material and the FeS–$W_{18}O_{49}$ composite as the cathode. Fig. 8a provides a schematic illustration of the ASC's structural design. Fig. 8b shows that FeS–$W_{18}O_{49}$ operates over a potential window from −0.8 to 0 V, while MnO_2 spans from 0.0 to 0.8 V, resulting in a maximum operating voltage of 1.6 V for the device. As shown in Fig. 8b, the capacitance curves exhibit a gradual increase in area at a constant scan rate, and the redox peaks display minimal visibility, indicating a strong correspondence between the positive and negative charges within the device. This suggests exceptional capacitive performance. The FeS–$W_{18}O_{49}$||MnO_2 capacitor performance is governed by a combination of electrical double-layer capacitance (EDLC) and faradaic pseudocapacitance mechanisms. As the scan rate increases from 10 mV s^{-1} to 50 mV s^{-1}, gradual changes in the cyclic voltammetry (CV) curves are observed, highlighting the superior capacitance and rate capabilities of the fabricated ASC devices. Fig. 8c presents the galvanostatic charge–discharge (GCD) curves of the FeS–$W_{18}O_{49}$||MnO_2 supercapacitor at different current densities. The device achieves specific capacitances of 202, 191, 129, 80, and 62 F g^{-1} at current densities of 1, 2, 3, 4, and 5 A g^{-1}, respectively (as shown in Fig. 8d and Table 4). The symmetrical nature of the GCD curves further indicates excellent electrochemical reversibility. Additionally, the impedance analysis in Fig. 8e provides further insights into the charge transport kinetics of the ASC. The steep slope of the linear portion of the plot confirms the remarkable capacitive characteristics of the FeS–$W_{18}O_{49}$||MnO_2 supercapacitor.

The feasibility of the FeS–$W_{18}O_{49}$||MnO_2 asymmetric supercapacitor (ASC) is primarily evaluated based on its energy and power densities. The magnitudes of these parameters are determined using eqn (3) and (4). At a current density of 1 A g^{-1}, the device achieves an energy density of 89.77 W h kg^{-1} and a power density of 997.4 W kg^{-1}. When the discharge current reaches 10 A g^{-1}, these values increase significantly to 27.5 W h kg^{-1} and 4950 W kg^{-1}, respectively. Table 4 provides a detailed summary of these values at various current rates. This

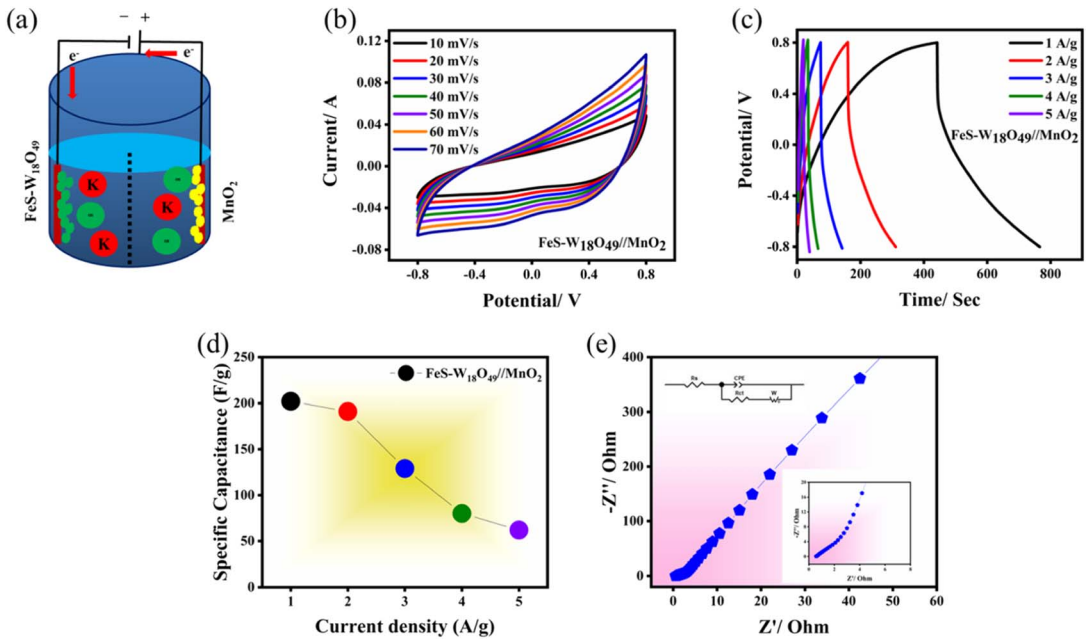

Fig. 8 Characteristics of the FeS–$W_{18}O_{49}$||MnO_2 ASC: (a) schematic illustration of the FeS–$W_{18}O_{49}$||MnO_2 device, (b) CV curve at 1.6 V, (c) GCD curves at 1–5 A g^{-1}, (d) specific capacitance as a function of current density, and (e) EIS plot.

Table 5 Comparative analysis of the electrochemical performance of iron against various composite materials

Composites	Specific capacitance F g^{-1}	Electrolyte	Potential window (V)	Cyclic retention	Reference
GA-FeS_2	313.6	6 M KOH	−0.9 to −0.3	88.2% @ 2000 cycles	24
FeS_2@Fe_2O_3	145	1 M $LiSO_4$	−1.0 to 0.0	95% @ 5000 cycles	25
FeS film	193	1 M $LiClO_4$	0.0 to 1.2	90% @ 1000	26
Fe_2O_3/N-rGO	137	1 M KOH	−1.0 to 0.0	95.8% @ 2000	27
Fe_2O_3-graphene	151.8	2 M KOH	−0.85 to 0.0	86% @ 2000	28
Poros Fe_2O_3	193	0.5 M Na_2SO_3	−0.8 to 0.0	92% @ 1000	29
FeOOH/ECTN	150	6 M KOH	−1.1 to 0.0	48% @ 3500	30
Fe_3O_4/CNF	135	1 M Na_2SO_3	−0.9 to 0.1	91% @ 1000	31
FeS/rGO/FeS	206.25	2 M KOH	−1.4 to 0.2	118% @ 5000	32
FeS–$W_{18}O_{49}$	202	3 M KOH	−0.8 to 0.8	87.6% @ 10 000	This work

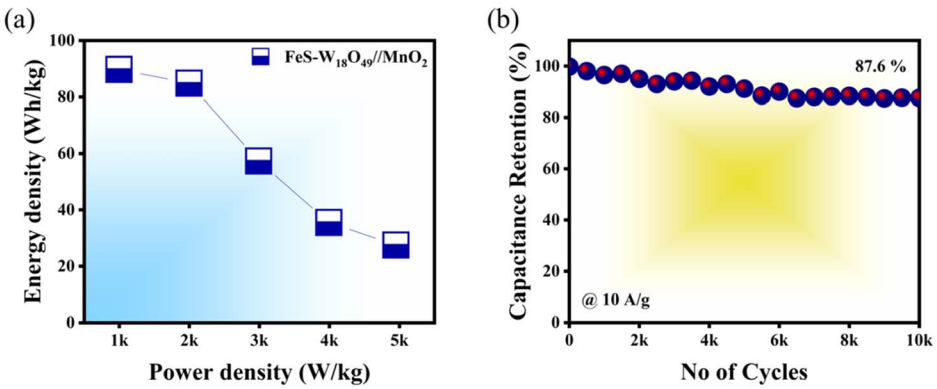

Fig. 9 (a) Ragone plot illustrating the energy and power density relationship of the FeS–$W_{18}O_{49}$||MnO_2 ASC. (b) Long-term cycling stability test at a high current density of 10 A g^{-1}.

study confirms the synergistic effect between FeS and $W_{18}O_{49}$ within the composite matrix, which facilitates efficient energy and power delivery. The interaction between these two materials leads to a composite with exceptional electrical conductivity. To determine the practical applicability of the FeS–$W_{18}O_{49}$||MnO_2 ASC, its cycling stability was assessed by subjecting it to 10 000 charge–discharge cycles at high current rates, as shown in Fig. 9b. The results indicate some structural degradation during the electrochemical cycling process, yet the device retains 87.6% of its initial capacitance after 10 000 cycles, even at elevated current rates (refer to Fig. 7b). This demonstrates the remarkable cycling stability of the FeS–$W_{18}O_{49}$||MnO_2 ASC, validating its potential for practical energy storage applications.

5. Conclusion

This study presents a cost-effective wet-chemical synthesis method for producing an FeS–$W_{18}O_{49}$ nanocomposite tailored for supercapacitor applications. The nanocomposite exhibits excellent charge retention through electric double-layer capacitance (EDLC) in an aqueous solution, facilitated by rapid faradaic redox reactions. Compared to the individual components, FeS and $W_{18}O_{49}$, the FeS–$W_{18}O_{49}$ electrode exhibits superior performance, achieving a specific capacitance of 558 F g^{-1} within a potential window of −0.8 to 0.0 V. The asymmetric supercapacitor (ASC) device, configured as FeS–$W_{18}O_{49}$||MnO_2 in a KOH electrolyte, extends the operating voltage window to 1.6 V and achieves a specific capacitance of 202 F g^{-1}, demonstrating outstanding rate capability. The material benefits from enhanced electrical conductivity and the synergistic interaction between Fe and W elements, supporting a prolonged cycling life exceeding 10 000 cycles. Compared to conventional electrode materials, the FeS– $W_{18}O_{49}$ nanocomposite delivers a remarkable energy density of 89.77 W h kg^{-1} at a maximum power density of 4950 W kg^{-1}, underscoring its potential as a highly efficient energy storage solution for next-generation supercapacitors.

Data availability

The data that have been used are confidential and will be available on request.

Conflicts of interest

The authors declare that they have no conflict of interest.

Acknowledgements

This research did not receive any specific grant from funding agencies in the public, commercial, or not-for-profit sectors.

References

1 N. A. Kyeremateng, T. Brousse and D. Pech, Microsupercapacitors as miniaturized energy-storage components for on-chip electronics, *Nat. Nanotechnol.*, 2017, **12**(1), 7–15.

2 D. P. Dubal, *et al.*, Synthetic approach from polypyrrole nanotubes to nitrogen doped pyrolyzed carbon nanotubes for asymmetric supercapacitors, *J. Power Sources*, 2016, **308**, 158–165.

3 S. Arulmani, C. Suresh and C. Sivakumar, 3D-Interconnected Channels of Ordered Mesoporous Carbon (3D-OMC): Effective Electrode Material for Electrochemical Supercapacitors, *Meet. Abstr.*, 2016, **229**(1).

4 J. Riaz, *et al.*, Facile synthesis of TiN nano sheets decorated Fe_2O_3 nanoparticles as novel cathode material for Asymmetric Supercapacitor, *Surface. Interfac.*, 2024, **46**, 104080.

5 F. Yu, L. Pang and H.-X. Wang, Preparation of mulberry-like RuO_2 electrode material for supercapacitors, *Rare Met.*, 2021, **40**, 440–447.

6 H. Shi, *et al.*, Preparation of petal-particle cross-linking flowerlike NiO for supercapacitor application, *J. Electroanal. Chem.*, 2020, **876**, 114481.

7 D. Wang, *et al.*, Nanostructured Fe_2O_3–graphene composite as a novel electrode material for supercapacitors, *J. Solid State Electrochem.*, 2012, **16**, 2095–2102.

8 J. Riaz, *et al.*, Improved performance of TiN nano buds decorated MoS_2 sheets in asymmetric supercapacitors, *J. Mater. Sci.: Mater. Electron.*, 2024, **35**(17), 1142.

9 G. S. Gund, C. D. Lokhande and Ho S. Park, Controlled synthesis of hierarchical nanoflake structure of NiO thin film for supercapacitor application, *J. Alloys Compd.*, 2018, **741**, 549–556.

10 S. Xiong, *et al.*, A high-performance hybrid supercapacitor with NiO derived NiO@Ni-MOF composite electrodes, *Electrochim. Acta*, 2020, **340**, 135956.

11 J. Riaz, *et al.*, Facile synthesis and electrochemical analysis of TiN-based ZnO nanoparticles as promising cathode materials for asymmetric supercapacitors, *Nanoscale Adv.*, 2024, **6**(20), 5145–5157.

12 N. Hassan, *et al.*, Vanadium oxide (V_2O_3) for energy storage applications through hydrothermal route, *J. Mater. Sci.: Mater. Electron.*, 2018, **29**, 16021–16026.

13 J. Jung and Do H. Kim, $W_{18}O_{49}$ nanowires assembled on carbon felt for application to supercapacitors, *Appl. Surf. Sci.*, 2018, **433**, 750–755.

14 J. Riaz, *et al.*, Hydrothermal synthesis of ball-like ZnS nanospheres decorated urchin-like $W_{18}O_{49}$ nanospheres as electrode for high power and stable hybrid supercapacitor, *Mater. Lett.*, 2024, **370**, 136853.

15 G. Murugadoss, S. Salla, and P. Arunachalam, Oxides free materials for symmetric capacitors, *Oxide Free Nanomaterials for Energy Storage and Conversion Applications*, Elsevier, 2022. pp. 75–94.

16 Y. Tian, *et al.*, Synergy of $W_{18}O_{49}$ and polyaniline for smart supercapacitor electrode integrated with energy level indicating functionality, *Nano Lett.*, 2014, **14**(4), 2150–2156.

17 S. Park, *et al.*, High-power and long-life supercapacitive performance of hierarchical, 3-D urchin-like $W_{18}O_{49}$ nanostructure electrodes, *Nano Res.*, 2016, **9**, 633–643.

18 N. R. Chodankar, *et al.*, A symmetric MnO_2/MnO_2 flexible solid state supercapacitor operating at 1.6 V with aqueous gel electrolyte, *J. Energy Chem.*, 2016, **25**(3), 463–471.

19 Q. Wang, *et al.*, $NiCo_2O_4$ nanowire arrays supported on Ni foam for high-performance flexible all-solid-state supercapacitors, *J. Mater. Chem. A*, 2013, **1**(7), 2468–2473.

20 J. Riaz, *et al.*, High-performance electrode material synthesis via wet-chemical method: a study on NbN–Fe_2O_3 composite, *J. Mater. Sci.: Mater. Electron.*, 2024, **35**(17), 1176.

21 Lichchhavi, *et al.*, Transformation of battery to high performance pseudocapacitor by the hybridization of $W_{18}O_{49}$ with RuO_2 nanostructures, *Langmuir*, 2021, **37**(3), 1141–1151.

22 Yu Hu, *et al.*, Nickel ion (Ni^{2+}) doping induced formation of $W_{18}O_{49}/W_3O_8$ bulk homojunction for enhancing photo-assisted energy storage, *J. Alloys Compd.*, 2024, **990**, 174506.

23 J. Riaz, *et al.*, Wet-chemical synthesized TiN-CuO nanocomposite: Advancing supercapacitor technology with high energy and power density, *Phys. E*, 2025, **165**, 116105.

24 L. Pei, *et al.*, Self-assembled flower-like FeS_2/graphene aerogel composite with enhanced electrochemical properties, *Ceram. Int.*, 2016, **42**(4), 5053–5061.

25 Y. Zhong, *et al.*, Hierarchical FeS_2 nanosheet@Fe_2O_3 nanosphere heterostructure as promising electrode material for supercapacitors, *Mater. Lett.*, 2016, **166**, 223–226.

26 S. S. Karade, *et al.*, First report on a FeS-based 2 V operating flexible solid-state symmetric supercapacitor device, *Sustain. Energy Fuels*, 2017, **1**(6), 1366–1375.

27 H. D. Liu, *et al.*, Easy one-step hydrothermal synthesis of nitrogen-doped reduced graphene oxide/iron oxide hybrid as efficient supercapacitor material, *J. Solid State Electrochem.*, 2015, **19**, 135–144.

28 D. Wang, *et al.*, Nanostructured Fe_2O_3–graphene composite as a novel electrode material for supercapacitors, *J. Solid State Electrochem.*, 2012, **16**, 2095–2102.

29 S. Shivakumara, T. Rao Penki and N. Munichandraiah, Preparation and electrochemical performance of porous hematite (α-Fe_2O_3) nanostructures as supercapacitor electrode material, *J. Solid State Electrochem.*, 2014, **18**, 1057–1066.

30 J. Li, *et al.*, FeOOH nanorod arrays aligned on eggplant derived super long carbon tube networks as negative electrodes for supercapacitors, *New J. Chem.*, 2018, **42**(6), 4513–4519.

31 J. Mu, *et al.*, Highly dispersed Fe_3O_4 nanosheets on one-dimensional carbon nanofibers: synthesis, formation mechanism, and electrochemical performance as supercapacitor electrode materials, *Nanoscale*, 2011, **3**(12), 5034–5040.

32 X. Shao, *et al.*, Hierarchical FeS/RGO/FeS@Fe foil as high-performance negative electrode for asymmetric supercapacitors, *Inorg. Chem. Front.*, 2018, **5**(8), 1912–1922.